286 Toward Reduced Transport Errors in a High Resolution Urban CO_2 Inversion System

Aijun Deng*, Thomas Lauvaux, Brian Gaudet, Tasha Miles, Kenneth J. Davis, Kai Wu and Daniel Sarmiento
Department of Meteorology, The Pennsylvania State University

Kevin R. Gurney
Arizona State University

Michael Hardesty, Tim Bonin and Alan Brewer
NOAA Earth Science Research Laboratory

1. INTRODUCTION

Inversion approach has been widely used to determine the improved surface flux of greenhouse gases (GHGs) such as CO_2, using the observed concentration from various platforms such as aircraft and towers. The components of inversion system include a forward transport model that represents the atmospheric transport processes, a backward model that determines the influence function for each observation site, and the inversion model that updates the fluxes based on the influence functions for all the observation sites. The forward transport model can be any atmospheric model such as a mesoscale numerical weather prediction (NWP) model. The backward model is typically an offline transport and dispersion model that is driven by the NWP model solutions and that runs backward in time (e.g., driver data is inputted in reverse order). The inversion model computes the updated fluxes based on influence functions, given estimated transport error and observation error.

The Weather Research and Forecasting (WRF) model, a state-of-the-science community-supported numerical weather prediction (NWP) and atmospheric simulation system, is used in this research as the forward transport model. WRF has been used worldwide for both research and operational applications (Skamarock et al. 2008), and has been proven to have good skill in accurately predict/simulate atmospheric processes relevant to atmospheric transport and dispersion applications (Cintineo et al. 2014, Clark et al. 2015, Coniglio et al. 2013, Hariprasad et al. 2014, Rogers et al. 2013, Lauvaux et al. 2013, Karion et al. 2015). In addition to its advanced numerical scheme and model physics that are still under development and continuous improvements, WRF has an four dimensional data assimilation (FDDA) capability implemented by Penn State University (Deng et al. 2009) that allows meteorological observations to be continuously assimilated to allow WRF to produce the dynamic analysis at user-desired resolution.

Using the WRF modeling system, Rogers et al. (2013) investigated effect of various FDDA strategies on the accuracy of the WRF-simulated mesoscale features over Central Valley, CA. The goal of that research was to develop an optimal model configuration to be used in the operational modeling system in Bay Area Air Quality Management District (BAAQMD). The optimal model settings in FDDA configuration has been used in many recent modeling studies involving studying GHGs (Lauvaux et al. 2013, Karion et al. 2015), and has shown to be able to produce accurate model solutions

In the Indianapolis Flux Experiment (INFLUX) research project, we plan to use the WRF model and its FDDA capability for multiple years to study the CO_2 emission and transport processes. However, we need first to understand the effect of assimilating various meteorological data on the transport model accuracy and the effect on the posterior CO_2 fluxes and to develop an optimal model configuration before we proceed with multi-year simulations. In this paper, we chose a 2-month time period in 2013 for the purpose of developing an optical model configuration, with focus on evaluating the effect of assimilating various meteorological observations on the WRF solutions, and its impact on the linearized adjoint solutions used in the CO_2 inversion system for INFLUX. Since World Meteorological Organization (WMO) upper-air observations are sparse in time (i.e., 12 hourly apart) and space (hundreds of kilometers apart), additional observations from different platforms were introduced, including the HALO lidar wind observations and aircraft measurements from the commercial airline program, Aircraft Communications Addressing and Reporting System (ACARS). We present the inverse CO_2 emissions over 2 months (September-October 2013) using different atmospheric simulations that assimilate surface stations, lidar, and ACARS, and assess the improvement in model performance based on the meteorological instrumentation used in our assimilation system. The data types assimilated includes 1) Standard WMO surface and upper-air observations, available hourly for surface and 12-hourly for upper air; 2) Wind profiles from the local HALO lidar deployed by NOAA Earth System Research Laboratory Chemical Sciences Division (http://www.esrl.noaa.gov/csd/groups/csd3/measurements/influx/) at Ivy Tech Community college in Indianapolis, available at 20-min. intervals; 3) ACARS commercial aircraft observations, available anywhere in space and time with low-level observations near the major airports.

In order to understand the effect of assimilating meteorological observations from various platforms on the posterior urban CO_2 fluxes updated by the high-resolution inversion system, we conducted several sensitivity studies and compared the meteorological solutions from WRF and the CO_2 fluxes from the

*Corresponding Author: Aijun Deng, Department of Meteorology, 503 Walker Building, Pennsylvania State University, University Park, PA 16802; email: axd157@psu.edu

inversion system. Section 2 describes the components of the inversion system used in this study. Model configurations and experimental design are discussed in Section 3. Model results and discussions are given in Section 4, and a summary and conclusions are given in Section 5.

2. MODEL DESCRIPTION

The Modeling system used in this research consists of a mesoscale atmospheric modeling component that handles transport and dispersion, a Lagrangian Particle Dispersion Model (LPDM) that is run backward and driven by the solutions of the atmospheric transport model to calculate the influence functions needed for inversion, and the inversion modeling system to compute the posterior flux given the prior fluxes and influence functions as well as the estimates of transport model errors and observation errors. The mesoscale atmospheric model used here is the Weather Research and Forecasting (WRF) model, which is a state-of-the-science community-supported numerical weather prediction (NWP) and atmospheric simulation system. WRF has been used worldwide for both research and operational applications (Skamarock et al. 2008). WRF's development is supported by the broad scientific community, along with very active participation of university scientists worldwide. WRF has a flexible, portable code that runs efficiently in computing environments ranging from massively parallel supercomputers and clusters to laptops.

WRF is a non-hydrostatic, fully compressible three dimensional (3D) primitive equation model with a terrain-following, hydrostatic pressure vertical coordinate, and is designed for simulating atmospheric phenomena across scales ranging from large eddies (~100 m) to mesoscale circulations and waves (~ 1 km to 100 km) to synoptic-scale weather systems (~1000 km). These applications include real-time NWP, model physics research, regional climate simulation, air-quality and hazard prediction modeling with addition of a chemistry module (WRF-Chem, Grell et al. 2005), etc.

The WRF model includes a complete suite of atmospheric physical processes that interact with the model's dynamics and thermodynamics core. These physical processes include cloud microphysics (MP), cumulus parameterization needed on coarser grids (dx > O(10km)) for representing the un-resolved atmospheric convection, atmospheric radiation, planetary boundary layer (PBL)/turbulence physics, and land surface models (LSMs). Selection of model physics suite in this research is based on the similar modeling studies that were conducted previously (e.g., Lauvaux et al. 2013, Rogers et al. 2013). For microphysics, this study uses the WRF single-moment five-class (WSM5) simple ice scheme (Hong et al. 2004) that assumes no mixed-phase conditions. For cumulus parameterization, the Kain–Fritsch scheme (Kain and Fritsch 1990, 1993; Kain 2004) is used on the 9-km grid (see next section for grid configuration). For atmospheric radiation, the Rapid Radiative Transfer Model (RRTM; Mlawer et al. 1997) longwave (LW)/Dudhia shortwave (SW; Dudhia 1989) scheme is used. For PBL turbulent processes, the turbulent kinetic energy (TKE)-predicting Mellor-Yamada Nakanishi Niino (MYNN) Level 2.5 turbulent closure scheme (Nakanishi and Niino 2006) is used, along with the MYNN surface layer scheme to preserve consistence. The decision on selecting the MYNN PBL scheme is based on the fact that MYNN appeared to produce most accurate temperature and moisture profiles (Cintineo et al. 2014, Clark et al. 2015,) and most accurate PBL depth (Coniglio et al. 2013, Hariprasad et al. 2014), most important to transport and dispersion applications . For land surface processes, the Noah LSM (Chen and Dudhia 2001, Tewari et al. 2004) is used. The Noah LSM is a four-layer soil temperature and moisture scheme and includes root zone, evapotranspiration, soil drainage, and runoff, taking into account vegetation categories, monthly vegetation fraction, and soil texture. The scheme can predict soil ice and snow cover.

The WRF modeling system also has four dimensional data assimilation (FDDA) capabilities that allow continuous assimilation of meteorological observations into the modeling system as the model is running. For retrospective applications, FDDA can be used in numerical models to produce accurate dynamic analyses at the desired temporal and spatial resolution. FDDA has been widely used in studying atmospheric transport and dispersion processes (Deng et al. 2004, 2006, Rogers et al. 2013, Lauvaux et al. 2013, Karion et al. 2015). The version of FDDA used in this research was originally developed for MM5 at Penn State and was enhanced and implemented into WRF (Deng et al. 2009). Further enhancements to the observation, or obs, nudging technique in WRF have brought more flexibility to control how surface observations influence meteorology in aloft layers. WRF users have freedom to choose different vertical weighting functions for the surface observations (Rogers et al. 2013). Unlike Rogers et al. (2013) in which various FDDA strategies were evaluated to identify the optimal FDDA settings to produce the most accurate model solutions to represent the meteorological conditions, this research focus on exploring the effect of assimilating various meteorological observations on the model solution as well as on the solutions (i.e., posterior fluxes) of the inversion system that is driven by the WRF model solutions. The optimal model configuration will be used for multi-year urban inversion calculations over the INFLUX domain.

The LPDM (Uliasz, 1994) is used to calculate the influence functions. The input to the LPDM is the hourly 3-D wind fields simulated by the WRF model discussed above, except that the wind fields are inputted backwards in time so that areas of influence for a given tower observation can be estimated. The input to LPDM also includes the WRF-predicted turbulent kinetic energy (TKE) representing the strength of the turbulent mixing needed for vertical diffusion calculation in the LPDM.

In the inversion system we use the influence function for each tower location determined by LPDM calculation and the observed CO_2 concentrations from the 12 INFLUX towers, to compute the posterior fluxes.

3. MODEL CONFIGURATION AND EXPERIMENTAL DESIGN

The WRF modeling system used in this research is based on WRF V3.5.1, released in September 2013. The INFLUX WRF configuration consists three nested grids with 9-/3-/1-km horizontal resolutions (Fig. 1), with the focus on the 1-km grid. The topographic and landuse database needed to initialize the WRF model are based on the U.S. Geological Survey (USGS) 30-seceond terrain and 24-category landuse. As indicated by the landuse distributions (Fig. 2), Indianapolis region is represented as an urban category, and a significant fraction of the 1-km grid is characterized as urban. In the vertical, fifty nine (59) vertical terrain-following layers are used, with the center point of the lowest model layer located ~7 m above ground level (AGL). The thickness of the layers increases gradually with height, with 24 layers below 850 hPa (~1550 m AGL). The top of the model is set at 100 hPa. The initial and boundary conditions are based on North America Regional Reanalysis (NARR).

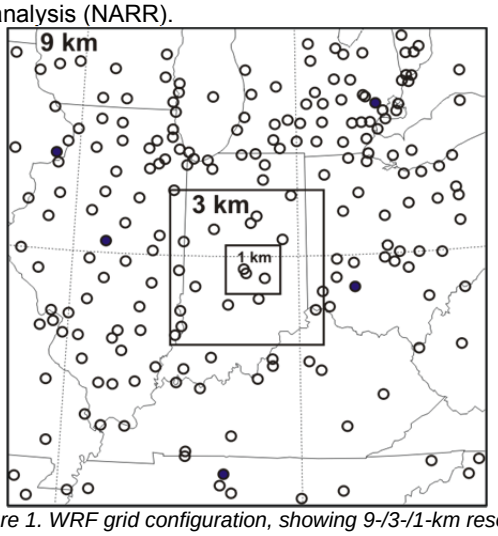

Figure 1. WRF grid configuration, showing 9-/3-/1-km resolution grids

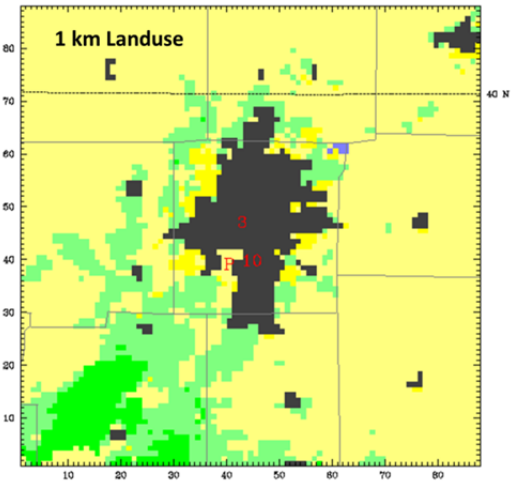

Figure 2. WRF landuse map on the 1-km resolution grid. Locations of INFLUX site 3 and 10 are also shown, and 'P' indicates the location of the Harding street power plant

WRF-Chem system was configured to run for a two-month period (Sept.-Oct. 2013), in 5-day segments with a 12-hour overlapping time-window. The WRF model solutions are then used to drive a Lagrangian Particle Dispersion Model (LPDM) that calculates the CO_2 footprints for each of the CO_2 tower observations. The footprints or influence functions are used to in the inversion system to compute the updated posterior CO_2 fluxes. During the model simulation time window, meteorological observations are assimilated into the WRF model to produce the most accurate meteorological conditions. The meteorological observations assimilated include the standard measurements of wind, temperature and moisture fields from WMO surface stations at hourly intervals and radio sondes at 12-houly intervals. The winds measured from the INFLUX lidar at 20-minute intervals are also available for assimilation. In addition to the WMO and INFLUX observations, the winds, temperatures and moisture fields observed from the Aircraft Communications Addressing and Reporting System (ACARS) are also assimilated. The ARCARS observations are available at any random times when observations are taken. Distributions of the assimilated WMO observations are demonstrated in Fig. 1. As mentioned earlier, these in-situ observations are continuously assimilated using the WRF FDDA technique that is described in Deng et al. (2009) and Rogers et al. (2013). Same as in the previous studies (i.e., Deng et al. 2004, 2006, Rogers et al. 2013, Lauvaux et al. 2013, Karion et al. 2015), assimilation of temperature and moisture observations are only allowed above the model-predicted PBL top so that the PBL physics processes in the model are dominated by the thermodynamics without interference from the data assimilation, while winds are assimilated through the entire atmosphere.

In order to evaluate the effect of assimilating various observation sources, as shown in Table 1, four different WRF experiments are conducted, and results of both meteorological fields and posterior CO_2 fluxes are evaluated for these experiments: 1) NOFDDA – No data assimilation of any form is applied and WRF is purely driven by NARR; 2) FDDA_WMO – Only standard WMO hourly surface and 12-hourly upper-air observations are assimilated; 3) FDDA_WMO_Lidar – In additional to WMO observations, wind profiles from the local INFLUX HALO lidar are also assimilated; and 4) FDDA_WMO_Lidar_ACARS – In additional to the WMO and lidar observations, the ACARS observations are also assimilated. As shown in Fig. 1, there are five upper-air observations spread across the 9-km grid. However, none of them are located on the 3- and 1-km grids and only three WMO stations are available on the 1-km grid; thus the benefit of assimilating WMO sondes can only propagate through the grid boundaries into the 3- and 1-km grids. Since the surface observations can only affect the lowest portion of atmosphere up to the model-simulated PBL top (Deng et al. 2009), it is anticipated that assimilating additional upper air observations such as Lidar and ACARS observations can further improve the WRF model solutions so that the

transport error in the inversion system is further reduced. The goal of is paper is to demonstrate the effect of assimilating observation from various sources on both the meteorological model and inversion solutions.

Table 1: Experimental Design

Exp. Name	Description
NOFDDA	No meteorological observations of any form are assimilated
FDDA_WMO	Assimilating only WMO surface observations and upper-air sondes
FDDA_WMO_Lidar	Same as above with assimilation of INFLUX HALO lidar winds
FDDA_WMO_Lidar_ACARS	Same as above with assimilation of ACARS wind and mass fields

All experiments use the identical model physics for all grids except that cumulus parameterization scheme is applied only on the 9-km grid. For land surface process, 4-layer Noah land surface model (Tewari et al. 2004) is used. The 2.5-level MYNN scheme (Nakanishi and Niino 2006) is use to represent the PBL turbulence. The RRTM radiation scheme (Mlawer et al. 1997) is used for both longwave and Dudhia scheme (Dudhia 1989) is used for shortwave. KF cumulus scheme (Kain and Fritsch 1990, 1993, Kain 2004) is used. For the preliminary evaluations conducted in this paper, each WRF simulation segment of the four experiments are 5-day long, and was initialized with 3-hourly North America Regional Reanalysis (NARR) analyses at 40x40-km resolution for the initial conditions and lateral boundary conditions (ICs/LBCs). The NARR analyses were downloaded from the Research Data Archive (RDA) maintained by the Computational and Information Systems Laboratory (CISL) at the National Center for Atmospheric Research (NCAR).

In addition to assimilating observations during the model integration, the IC fields are further enhanced by rawinsonde and surface data through the WRF objective analysis process, Obsgrid, using a modified Cressman analysis method (Deng et al. 2009, Rogers et al. 2013). The three-dimensional (3-D) analyses and the surface analysis fields used for analysis FDDA are also enhanced by the objective analysis process and are defined at three-hour intervals.

For the chemistry initialization with CO_2, Hestia 2012 product (Gurney et al. 2012) was used to determine the emission values.

4 MODEL RESULTS

4.1 Meteorological Evaluation

The WRF-simulated meteorological fields are evaluated quantitatively by comparing the error statistical scores of the model-simulated wind speed, wind direction, and temperature T. Evaluation is performed on the 1-km grid only since the high-resolution grid is our primary interest. Mean absolute error (MAE) and root mean square error (RMSE) are calculated to measure how close the model values are compared to the observed values. Mean error (ME) is calculated to measure the model bias for a given variable. MAE and ME are computed for both the surface and upper air observation locations separately. For the surface, the WRF (2-m temperature and 10-m wind) values derived from the lowest model layer using the similarity theory are compared with the surface observations. For the upper air, the model values are interpolated onto the observation locations in both horizontal and vertical pressure space, and are then compared with the observations. A calm wind threshold was used in this study to remove the very light winds (less than or equal to 1 m s^{-1}) for the wind direction statistics calculation because the wind direction for near-calm wind is uncertain.

Table 2 shows the ME and MAE of the WRF-predicted 10-m wind direction, wind speed and 2-m temperature over the 1-km grid verified hourly against three WMO surface measurements, averaged over the period between 00 UTC 27 August and 00 UTC 3 November 2013. Comparing the model surface MAE and ME scores among all four numerical experiments, we notice that most error reductions occurs between experiments NOFDDA and FDDA_WMO. Surface wind direction MAE (ME) is reduced from 30 to 19 (6 to 2) degrees, and surface wind speed MAE is reduced from 1.0 to 0.8 (0.2 to 0.1) m s^{-1}. Since Lidar and ACARS observations are all taken above the surface, assimilating lidar and ACARS does not directly improve the surface MAE and ME scores for experiments FDDA_WMO_Lidar and FDDA_WMO_Lidar_ACARS. The MAE and ME scores for both experiments remain similar to the FDDA_WMO experiment (e.g., 19 degree wind direction MAE, 0.8 m s^{-1} MAE for both experiments). Although some slight degradation from the FDDA_WMO experiment is noticed in wind speed and temperature ME scores in FDDA_WMO_Lidar_ACARS experiment, it has the overall smallest MAE scores out of all four experiments. There are little temperature improvements since temperature assimilation is only allowed above the model-predicted PBL.

Table 2. Mean error and mean absolute error of the WRF-predicted 10-m wind direction, wind speed and 2-m temperature over the 1-km grid verified hourly against three WMO surface measurements, averaged over the period between 00 UTC 27 August and 00 UTC 3 November 2013.

		NOFDDA	FDDA_WMO	FDDA_WMO_Lidar	FDDA_WMO_Lidar_ACARS
Wind Direction	ME	6	2	2	1
	MAE	30	19	19	19
Wind Speed	ME	0.2	0.1	0	-0.2
	MAE	1.0	0.8	0.8	0.8
Temperature	ME	-1.0	-0.8	-0.9	-1.4
	MAE	2.3	2.3	2.4	2.2

Table 3. Mean error and mean absolute error of the WRF-predicted wind direction, wind speed and temperature over the 1-km grid verified hourly against the low-level (below 2 km AGL) INFLUX lidar measurements (winds only) and ACARS measurements (winds and temperatures), averaged over the period between 00 UTC 27 August and 00 UTC 3 November 2013.

		NOFDDA	FDDA_WMO	FDDA_WMO_Lidar	FDDA_WMO_Lidar_ACARS
Wind Direction	ME	4	2	-1	0
	MAE	26	24	15	14
Wind Speed	ME	0.2	-0.2	-0.2	-0.2
	MAE	2.0	2.0	1.3	1.2
Temperature	ME	0.8	1.0	1.0	0.5
	MAE	1.3	1.4	1.4	0.8

Table 3 shows ME and MAE of the WRF-predicted wind direction, wind speed and temperature over the 1-km grid verified hourly against the low-level (below 2 km AGL) INFLUX lidar measurements (winds only) and ACARS measurements (winds and temperatures) between, averaged over the period between 00 UTC 27 August and 00 UTC 3 November 2013. The information shown in Table 3 is the same as Table 2 except that validations are now performed against all upper air measurements, or all available measurements excluding the three surface stations. Now we clearly see that error reduction gradually occurs from the left (expt. NOFDDA) to the right (expt. FDDA_WMO_Lidar_ACARS), as additional observations are assimilated into the WRF model. For wind direction, the MAE (ME) scores reduces from 26 (4) degrees in NOFDDA experiment, to 24 (2) in degrees in FDDA_WMO experiment, and to 15 (-1) degrees in FDDA_WMO_Lidar experiment, and to 14 (0) degrees in FDDA_WMO_Lidar_ACARS experiment. For wind speed, the MAE (ME) scores are 2 (0.2) m s^{-1} in NOFDDA experiment, to 2 (-0.2) in m s^{-1} in FDDA_WMO experiment, and to 1.3 (-0.2) m s^{-1} in FDDA_WMO_Lidar experiment, and to 1.2 (-0.2) m s^{-1} in FDDA_WMO_Lidar_ACARS experiment. For temperature, the MAE (ME) scores are 1.3 (0.8) °C in NOFDDA experiment, to 1.4 (1.0) in °C in FDDA_WMO experiment, and to 1.4 (1.0) °C in FDDA_WMO_Lidar experiment, and to 0.8 (0.5) °C in FDDA_WMO_Lidar_ACARS experiment. Notice that MAE and ME scores are about the same between FDDA_WMO and NOFDDA, although there are slight degradation in temperature and slight improvement in wind direction in expt. FDDA_WMO from expt. NOFDDA. This is expected since there are no upper air WMO observations available on the 1-km grids. The increments in model errors (either improvement in wind direction or degradation in temperature) are caused by information propagated from the mother grids (i.e., 9- and 3-km grids).

As shown in Table 3, more evident error reductions in both MAE and ME are noticed between FDDAA_WMO and FDDA_WMO_Lidar where the INFLUX lidar wind measurements are assimilated. For example, there is a 9-degree error reduction in wind direction MAE and 0.7 m s^{-1} error reduction in wind speed MAE. There are no temperature improvements since no temperature observations are available from the INFLUX lidar. Assimilation or ACARS observations further reduces model MAE and ME error consistently in both wind and temperature fields except for wind speed ME which is already very small. For example, there is a 0.5 °C ME reduction and 0.6 °C MAE reduction in temperature when ACARS observations are assimilated. Same as indicated in the surface error statistics, expt. FDDA_WMO_Lidar_ACARS overall has the smallest error.

Comparing between NOFDDA and FDDA_WMO_Lidar_ACARS, we notice the improvement due to assimilating observations is evident and error reduction is significant, especially for wind direction, but not for temperature since temperature assimilation is only allowed above the PBL. For upper air, it is shown that due to assimilation of upper air observations of winds from the INFLUX lidar and ACARS and temperatures from ACARS, model improvement is quite obvious, especially for wind speed and wind direction. Temperatures appear to have smaller improvement, likely due to the fact that temperatures are already quite accurate.

Model errors averaged in vertical and over the entire 2-month period do not represent the temporal and spatial error distributions, understanding of which is important to transport and dispersion modeling. Time series of model-simulated wind direction and wind speed MAE for the entire 5-day simulation segment starting 12

UTC, 23 Sep. 2013 (not shown) indicated that for wind direction error appears to show diurnal variations, and direction error is smaller during nighttime and larger during daytime. Larger wind direction error during daytime is reasonable since surface wind direction is strongly affected by the PBL vertical mixing that is not well represented in the model, while during the nighttime wind direction is more influenced by large-scale conditions. However the wind speed error does not appear to have (or appear to have weaker) diurnal variations. This is likely because at the nighttime stable conditions, wind speed is not well predicted by the numerical models. Nevertheless, for both wind direction and wind speed and for both daytime and nighttime, assimilating surface WMO observations clearly reduces model error.

We also examined the vertical MAE distributions for WRF-predicted wind direction and wind speed (not shown), averaged over time, comparing among four numerical experiments listed in Table 1. For both wind speed and wind direction, expt. NOFDDA has the largest error through the entire atmosphere below ~2km AGL (except for the wind speed between 1 and 2km where expt. FDDA_WMO appears to have larger error), with a ~30-degree wind direction error and 2.5 m s^{-1} wind speed at the surface. Model error generally decreases with height. Comparing expt. NOFDDA and expt. FDDA_WMO, we notice that assimilating WMO surface observations only improves the model-predicted winds in a quite deep layer (up to 2-km for wind direction and up to 1-km for wind speed). This is because the FDDA sub-model in WRF allows the influence of the surface observations spread to entire depth of the PBL depending on the stability regime (Deng et al. 2009, Roger et al. 2013). Addition of the INFLUX lidar winds further reduces model error throughout the entire layer below 2-km. The large gap between the FDDA_WMO and FDDA_WMO_Lidar seem to suggest that addition of upper air observations is more important in improving the model solutions than assimilating surface observations alone. It is clear that addition of ACARS observations further reduces model errors. The fact that the amplitude of error reduction is not as large should not suggest that ACARS is not as effective as INFLUX lidar. This is simply because the lidar assimilation has already brought the model errors down to a small magnitude so that ACARS does not contribute much. If we rearranged the experimental design to add the ACARS first (instead of the INFLUX lidar first), we would see larger contribution from the ACARS and smaller contribution from the INFLUX lidar. It is the assimilation of upper air observations overall that contribute larger error reduction than assimilating surface observations. The error distributions indicate that model improvement due to assimilation of surface and upper air observations all together is quite significant, with overall >10-degree improvement in wind direction and > 1 m s^{-1} improvement in wind speed.

4.2 Evaluation of Model-Predicted PBL Depth Using the Halo Doppler Lidar Data

In addition to wind speed and wind direction, one of the meteorological variables critical to the transport and dispersion calculation is PBL depth that defines the vertical extent of the well-mixed CO_2 concentration. WRF model can produce the diagnosed PBL depth from its PBL sub model or PBL scheme. Some PBL schemes compute PBL depth based on the model-predicted thermal profiles, while other schemes diagnose PBL depth based on the vertical profile of TKE predicted by the PBL scheme. This research uses the 2.5-level MYNN scheme (Nakanishi and Niino 2006) that predicts TKE. The PBL depth is determined by the gradient of TKE (i.e., the vertical location where TKE value drops off significantly). We can compare the model-predicted PBL-depth with the observed PBL depth to measure how well the model represents the PBL processes.

The Halo Doppler lidar directly measures line-of-sight velocities and backscatter intensity from aerosols and other scatterers. A description of the system is provided by Pearson et al. (2009). Using a suite of scans that repeat every 20 min, profiles of wind speed, wind direction, and velocity variances are derived from these measurements, which are used in conjunction with the Signal-to-Noise Ratio (SNR) to estimate the PBL depth. Here, the PBL depth is manually estimated for each 20-min time period and located at large gradients in SNR and where the vertical velocity variance becomes small (less than $\approx$0.1 m2 s-2). For the study time period (Sep. to Oct. 2013), the Halo lidar is available for use in model validation. As an example, a comparison of PBL structures between WRF simulations (Expt. NOFDDA and FDDA_WMO_Lidar_ACASRS) and the INFLUX lidar observations at Indianapolis for 29 and 30 August 2013 is made (not shown). Generally, the model-predicted TKE structures are highly correlated with the lidar-observed vertical velocity variances and large gradients in SNR. However, differences in the vertical extent of these the depth of mixing from the model output and observations, thus PBL depth as well, are apparent.

Table 4 compared the MAE and ME of the WRF-predicted PBL depth on the 1-km grid verified hourly against the Halo lidar estimates of PBL depth at the lidar site in Indianapolis. The evaluation of PBL depth is conducted only for the daytime period between 17 and 22 UTC when a well-mixed PBL is fully developed and quasi-stationary, for the 2-month period between 00 UTC 27 August and 00 UTC 3 November 2013. Nighttime comparisons were not performed since it is well known that model is not able well-represent the stable condition; thus the predicted PBL depth is uncertain and unreliable. Our results show that for all experiments the MAE of mode-predicted PBL depth is quite similar, in a range between 223 and 272 m, or ~10-15% of the fully-developed PBL depth. Assimilating meteorological observations reduces the MAE except for a ~10 m degradation in expt. FDDA_WMO, with expt. FDDA_WMO_Lidar showing improvement from expt. NOFDDA, and with expt. FDDA_WMO_Lidar_ACARS having the smallest MAE. For ME, expt. NOFDDA already has small bias, and assimilating surface WMO observations only produces degradation. Addition of

Doppler lidar and ACARS observation reduces the bias from expt. FDDA_WMO, with the expt. FDDA_WMO_Lidar_ACARS having smallest ME (i.e. -23m). These results again seem to promote the importance of assimilating upper air observations.

Table 4. Mean error and mean absolute error (m) of the WRF-predicted PBL depth on the 1-km grid verified hourly against the Indianapolis INFLUX lidar measurements between 17and 22 UTC, for the period between 00 UTC 27 August and 00 UTC 3 November 2013.

	NOFDDA	FDDA_WMO	FDDA_WMO_Lidar	FDDA_WMO_Lidar_ACARS
ME	25	103	83	-23
MAE	259	272	254	223

4.3 Evaluation of Inverse Emissions

Using the observed CO_2 concentrations from the 12 INFLUX towers shown in Fig. 3, the 5-day inverse emissions were computed using a Bayesian inversion system at 1km resolution over the urban area of Indianapolis. The inversion results for Expt. NOFDDA, FDDA_WMO and FDDA_WMO_Lidar were completed and compared here in this paper. Figure 4 shows the results over the two-month period (Sept-Oct 2013) for the whole-city emissions. The variability among the 3 inversion cases represents the impact of differences in the WRF simulations. The WRF-FDDA with Lidar represents the optimal configuration with lower errors in both wind speed and direction, and is considered here as the reference case. Overall, the inverse emissions over the two months vary from 80ktC for Hestia to 90-95ktC for the different inversion estimates. The differences of about 50ktC among the inverse estimates represents about 50% of the change in the emissions compared to Hestia.

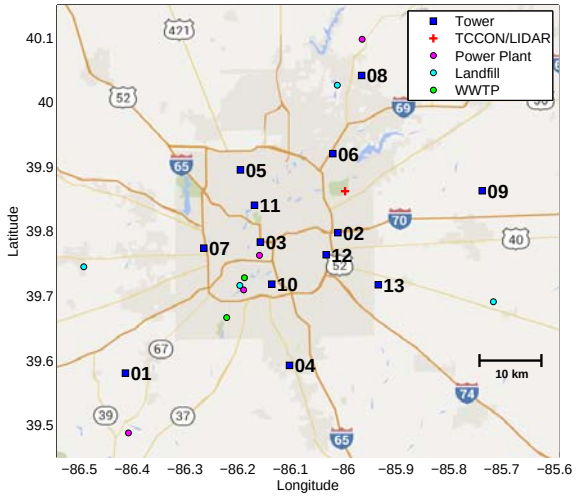

Figure 3. Observation network showing 12 INFXLU towers.

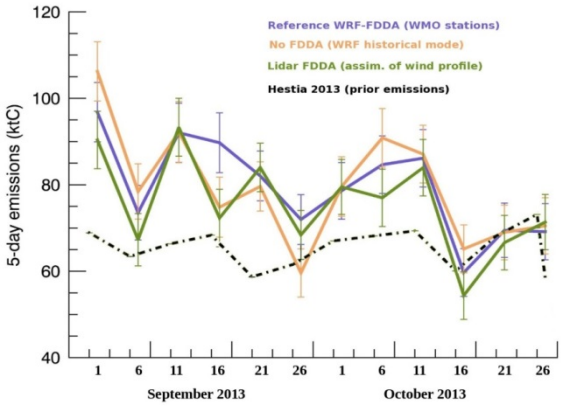

Figure 4. Five-day CO_2 emissions over Indianapolis using the three different WRF simulations. The Hestia CO_2 emissions were aggregated at 1km resolution and used as prior emissions in the inversion system (Gurney et al., 2012), indicated in black. The inverse emissions correspond to the 3 configurations described above with WRF in historical mode (NOFDDA, in orange), assimilating the WMO stations (FDDA-WMO, in purple), and assimilating the WMO and the HALO Lidar data (FDDA-WMO_Lidar, in green).

The Lagrangian Particle Dispersion Model (Uliasz 1994) was coupled to the WRF model over the two-months (Sept-Oct 2013). Particles were released continuously from the 12 tower locations in backward mode to simulate the area at the surface which directly influences the atmospheric concentrations. The footprints for 24 September 2013 are shown in Figure 5. The variability of the surface influence functions correspond to the differences in both wind speed (extent of the footprints along the main wind direction) and wind direction (width of the footprints). For this particular day, the wind direction varies only slightly between the three configurations whereas the wind speed was too high without the use of the FDDA system.

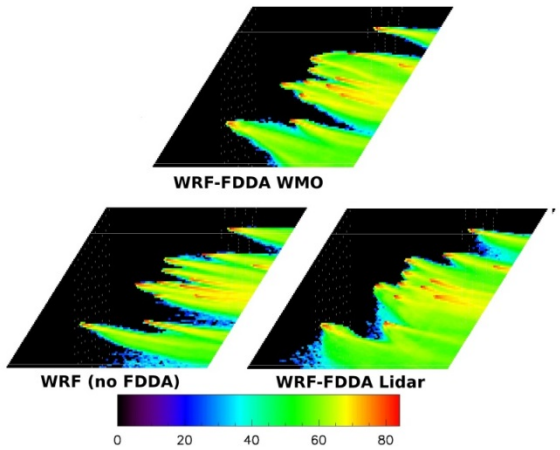

Figure 5. Influence functions over Indianapolis at 1km resolution for the 12 tower locations of the INFLUX network using the LPDM (Uliasz et al., 1994), for 24 September 2013 (aggregated over 17-22UTC) driven by the meteorological variables from the three different WRF configurations, in ppm_day/(g/m2/hour).

5. SUMMARY AND CONCLUSIONS

Our results indicate that model error can be significantly reduced by assimilating WMO observations. However, the assimilation of the WMO surface stations has a limited impact in the vertical (up to 900m max.). The assimilation of the wind profiles from the HALO lidar improved the WRF simulated wind speed and direction up to 2km high. The model performances were further increased due to the assimilation of ACARS data, filling the gaps between the 12-hourly WMO radiosondes and providing a better spatial density than the Lidar data.

It was found that inverse emissions from the three simulations are significantly impacted by the quality of transport simulations, with a difference of 50% in the emission correction after inversion depending on the transport simulations. The use of meteorological data improved the model performances and provided more robust CO_2 emissions at the city-scale, reducing the systematic errors in the inverse emissions. Therefore, we highly recommend the use of meteorological assimilation systems for high resolution inversions to avoid the propagation of systematic errors from the transport model into the emission estimates.

***Acknowledgement*:** This research is funded by the National Institute of Standards and Technology (NIST).

6. REFERENCES

Chen, F., and J. Dudhia, 2001: Coupling an advanced land surface-hydrology model with the Penn State–NCAR MM5 modeling system. Part I: Model implementation and sensitivity. Mon. Wea. Rev., 129, 569–585.

Cintineo, R., Jason A. Otkin, Ming Xue, and Fanyou Kong, 2014: Evaluating the Performance of Planetary Boundary Layer and Cloud Microphysical Parameterization Schemes in Convection-Permitting Ensemble Forecasts Using Synthetic GOES-13 Satellite Observations. Mon. Wea. Rev., 142, 163-182. doi: http://dx.doi.org/10.1175/MWR-D-13-00143.1

Clark, A. J., Michael C. Coniglio, Brice E. Coffer, Greg Thompson, Ming Xue, and Fanyou Kong, 2015: Sensitivity of 24-h Forecast Dryline Position and Structure to Boundary Layer Parameterizations in Convection-Allowing WRF Model Simulations. Wea. Forecasting, 30, 613-638. doi: http://dx.doi.org/10.1175/WAF-D-14-00078.1

Coniglio, M., C., James Correia Jr., Patrick T. Marsh, and Fanyou Kong, 2013: Verification of Convection-Allowing WRF Model Forecasts of the Planetary Boundary Layer Using Sounding Observations. Wea. Forecasting, 28, 842-862. doi: http://dx.doi.org/10.1175/WAF-D-12-00103.1

Deng, A. and D. R. Stauffer, 2006: On improving 4-km mesoscale model simulations. J. Appl. Meteor., 45, 361-381.

Deng, A., N. L. Seaman, G. K. Hunter and D. R. Stauffer, 2004: Evaluation of interregional transport using the MM5-SCIPUFF system. J. Appl. Meteor., 43, 1864-1886.

Deng, A., D.R. Stauffer, B.J. Gaudet, J. Dudhia, J. Hacker, C. Bruyere, W. Wu, F. Vandenberghe, Y. Liu and A. Bourgeois, 2009: Update on WRF-ARW end-to-end multi-scale FDDA system, 10th Annual WRF Users' Workshop, Boulder, CO, June 23, 14 pp (Available on the web at: http://www.mmm.ucar.edu/wrf/users/workshops/WS2009/abstracts/1-09.pdf).

Dudhia, J., 1989: Numerical study of convection observed during the Winter Monsoon Experiment using a mesoscale two–dimensional model. J. Atmos. Sci., 46, 3077-3107.

Grell, G. A., S. E. Peckhama, R. Schmitzc, S. A. McKeenb, G. Frostb, W. C. Skamarockd, B. Edere, 2005: Fully coupled "online" chemistry within the WRF model, Atmos. Environ. 39, 6957-6975, doi:10.1016/j.atmosenv.2005.04.027.

Gurney, K. R., I. Razlivanov, Y. Song, Y. Zhou, B. Benes, M. Abdul-Massih, 2012: Quantification of fossil fuel CO_2 emissions at the building/street scale for a large US city. Environmental Science & Technology, 2012; 120815073657007 DOI: 10.1021/es3011282.

Hariprasad, K.B.R.R., Srinivas, C.V., Bagavath Singh, A., Vijaya Bhaskara Rao, S., Baskaran, R., Venkatraman, B., 2014. Numerical simulation and intercomparison of boundary layer structure with different PBL schemes in WRF using experimental observations at a tropical site. Atmos. Res. 145, 27e44.

Hong, Song–You, Jimy Dudhia, and Shu–Hua Chen, 2004: A revised approach to ice microphysical processes for the bulk parameterization of clouds and precipitation. Mon. Wea. Rev., 132, 103-120.

Kain, J. S. and J. M. Fritsch, 1990: A one-dimensional entraining/detraining plume model and its application in convective parameterization. J. Atmos. Sci., 47, 2784-2802.

Kain, J. S. and J. M. Fritsch, 1993: Convective parameterization in mesoscale models: the Kain-Fritsch scheme. The representation of cumulus convection in numerical models, AMS. Monograph, K.A. Emanuel, and D. J. Raymond, EDS., 165-170.

Kain, J. S, 2004: The Kain-Fritsch convective parameterization: An update, J. Appl. Meteor, 43, 170-181.

Karion, A., C. Sweeney, E. A. Kort, P. B. Shepson, A. Brewer, M. Cambaliza, S. A. Conley, K. Davis, A. Deng, M. Hardesty, S. C. Herndon, T. Lauvaux, T. Lavoie, D. Lyon, T. Newberger, G. Pétron, C. Rella, M. Smith, S. Wolter, T. I. Yacovitch, and P. Tans, 2015: Aircraft-based estimate of total methane emissions from the Barnett Shale region, Environ. Sci. Technol., 49, 8124−8131, DOI: 10.1021/acs.est.5b00217.

Lauvaux T., N. L. Miles, S. J. Richardson, A. Deng, D. Stauufer, K. J. Davis, G. Jacobson, C. Rella, G.-P. Calonder, and P. L. DeCola, 2013: Urban emissions of CO_2 from Davos, Switzerland: the first real-time monitoring system using an atmospheric inversion technique. J. Appl Meteor. and Climatol., 52, 2654-2668.

Mlawer, Eli. J., Steven. J. Taubman, Patrick. D. Brown, M. J. Iacono, and S. A. Clough (1997), Radiative transfer for inhomogeneous atmospheres: RRTM, a validated correlated–k model for the longwave. J. Geophys. Res., 102, 16663-16682.

Nakanishi, M., and H. Niino, 2006: An improved Mellor-Yamada level 3 model: its numerical stability and application to a regional prediction of advecting fog. Bound. Layer Meteor. 119, 397-407.

Pearson, G., F. Davies, C. Collier, 2009: An analysis of the performance of the UFAM pulsed Doppler lidar for observing the boundary layer. J. Atmos. Oceanic Technol., 26, 240-250.

Rogers, R. E., A. Deng, D. R. Stauffer, B. J. Gaudet, Y. Jia, S. Soong, S. Tanrikulu, 2013: Application of the Weather Research and Forecasting Model for Air Quality Modeling in the San Francisco Bay Area. J. Appl. Meteor., 52, 1953-1973.

Skamarock, W.C., Klemp, J.B., Dudhia, J., Gill, D.O., Barker, D.M., Duda, M.G., Huang, X.-Y., Wang, W., Powers, J.G., 2008. A description of the Advanced Research WRF Version 3. NCAR Technical Note NCAR/TN-475+STR. 113 pp.

Tewari, M., F. Chen, W. Wang, J. Dudhia, M. A. LeMone, K. Mitchell, M. Ek, G. Gayno, J. Wegiel, and R. H. Cuenca, 2004: Implementation and verification of the unified NOAH land surface model in the WRF model. 20th conference on weather analysis and forecasting/16th conference on numerical weather prediction, pp. 11-15.

Uliasz, M., 1994: Lagrangian particle modeling in mesoscale applications, in Environmental Modelling II, edited by P. Zanetti, pp. 71-102, Computational Mechanics Publications, Southampto.